



**HAL**  
open science

# Influence of a rescanning strategy with different laser powers on the microstructure and mechanical properties of Hastelloy X elaborated by powder bed fusion

Clément Keller, M. Mokhtari, Benoît Vieille, H. Briatta, P. Bernard

## ► To cite this version:

Clément Keller, M. Mokhtari, Benoît Vieille, H. Briatta, P. Bernard. Influence of a rescanning strategy with different laser powers on the microstructure and mechanical properties of Hastelloy X elaborated by powder bed fusion. *Materials Science and Engineering: A*, 2021, 803, pp.140474. 10.1016/j.msea.2020.140474 . hal-03133794

**HAL Id: hal-03133794**

**<https://hal.science/hal-03133794>**

Submitted on 13 Feb 2023

**HAL** is a multi-disciplinary open access archive for the deposit and dissemination of scientific research documents, whether they are published or not. The documents may come from teaching and research institutions in France or abroad, or from public or private research centers.

L'archive ouverte pluridisciplinaire **HAL**, est destinée au dépôt et à la diffusion de documents scientifiques de niveau recherche, publiés ou non, émanant des établissements d'enseignement et de recherche français ou étrangers, des laboratoires publics ou privés.



Distributed under a Creative Commons Attribution - NonCommercial 4.0 International License

# Influence of a rescanning strategy with different laser powers on the microstructure and mechanical properties of Hastelloy X elaborated by powder bed fusion.

C. Keller<sup>a,\*</sup>, M. Mokhtari<sup>a</sup>, B. Vieille<sup>a</sup>, H. Briatta<sup>a</sup>, P. Bernard<sup>b</sup>

<sup>a</sup>*Groupe de Physique des Matériaux, UMR CNRS 6634, Normandie Université, avenue de l'Université, 76800 Saint-Etienne du Rouvray, France*

<sup>b</sup>*ArianeGroup, Forêt de Vernon, 27200 Vernon, France.*

---

## Abstract

The present study investigates the influence of a rescanning strategy on the microstructure and mechanical properties of Hastelloy X samples manufactured by laser powder bed fusion process in additive manufacturing. After a first lasing leading to powder melting, a second lasing is performed on the solid metal with five considered laser powers corresponding to 100-80-60-40 and 20% of the power of the first laser scan. The microstructure and mechanical properties of the samples obtained from these elaboration strategies were then compared to those of a conventional strategy with and without heat treatment. Using electron microscopy, monotonic and loading/unloading tensile tests, the results revealed that samples elaborated with the rescanning strategy are characterized by weaker crystallographic texture, lower back-stress and larger ductility compared to conventional elaboration parameters. However, these modifications induced by the second laser scan, depend on the second laser scanning power, better properties are observed for a decrease of 40% in the laser power during the second laser scan. Such strategy may be suitable to optimize the mechanical properties but also to potentially avoid post-elaboration heat treatments.

*Keywords:* Additive manufacturing, powder bed fusion, Superalloys, lasing strategy, mechanical properties, texture

---

\*Corresponding author, [clement.keller@insa-rouen.fr](mailto:clement.keller@insa-rouen.fr), +33232959865

## 1. Introduction

Due to its layer by layer manufacturing strategy, Additive Manufacturing (A.M.) is a major breakthrough over the last decades on the elaboration technique of metal parts with complex shapes. Among the different existing technologies, Laser Powder Bed Fusion (P.B.F.) is one of the most employed industrially.

Nevertheless, this technique is still very challenging for the metallurgical and mechanical communities. Indeed, the overall quality of parts obtained from P.B.F. depends on the process parameters such as the laser power and speed, the hatch distance, the powder layer thickness, the laser focus . . . [1]. The building strategy based on the laser path in a given layer but also with respect to the previous layer also plays an important role on the microstructure and mechanical characteristics of the manufactured part [2–6]. Depending on these parameters and building strategy, mechanical properties may be considerably affected due to a significant porosity rate, lack of powder fusion, overheating, crystallographic texture, morphological texture . . . [1; 7]. It is hence of prime importance to correctly understand the role played by the manufacturing parameters on the microstructure and properties to improve the process reliability but also the mechanical performance of metal parts obtained by additive manufacturing.

Due to aforementioned induced defects, metal parts obtained by AM are generally subjected to post-elaboration Heat Treatments (H.T.), sometimes coupled with mechanical loading (for instance Hot Isostatic Pressure - HIP), to reduce the residual stresses, the mechanical anisotropy and yield stress [1]. However these thermomechanical treatments increase both the overall elaboration time and costs limiting, hence, the interest of AM compared to conventional forming processes. Elaboration strategies which do not require further thermal or mechanical treatments deserve hence specific investigations. Moreover, depending on the industrial applications of the final part elaborated by AM, different mechanical properties may be desired at different locations. In the case of forged parts, these mechanical behavior modifications are obtained by local heat treatments using inductors for instance. For additive manufacturing parts, similar modifications of mechanical properties may be achieved from a local modification of the building strategy which ultimately influences the microstructure and the mechanical properties.

In literature, different strategies have been reported to increase the mechanical properties without H.T. . Besides the elaboration of optimized laser path for residual stresses reduction [3; 6], scanning strategies based on one or several laser rescans after the melting of a given powder layer has gained interest in the recent years. Indeed, despite a significant building time increase, that kind of elaboration strategy has been proved to improve the mechanical properties particularly in aluminum alloys, titanium alloys and stainless steels. Hence, it has been reported that the rescanning methods result in a decrease in residual stresses [8–12], a decrease in porosity rate [13; 14], a decrease in surface roughness [14–16], an increase in hardness [16] or ultimate tensile strength [17] and a modification of the microstructure [18]. However, these improvements seem to depend on the number of laser rescanning [12; 17], laser speed [9; 11], laser power [10; 11] and laser path during the successive laser scan on a given layer [17].

All these works point out the interest of rescanning strategies which may help to improve the microstructure and mechanical properties of metallic parts obtained by A.M. . However, for Ni superalloys, to the authors' best knowledge no investigation of such re-melting strategies has been published despite the huge industrial interest of these materials. Several questions still arise from these works, i) are rescanning strategies suitable for Ni superalloys ? ii) what is the effect of the power during the second laser scan ? iii) is remelting necessary for properties improvements ? iv) what is the influence of rescanning on microstructure? and v) what is the origin of these improvements ?

Thus, the aim of this article is hence to try to answer to these questions by investigating the role played by laser rescanning with different powers during a P.B.F. manufacturing on the microstructure and mechanical properties of a Hastelloy X superalloy. Such rescanning strategy, depending on its application (i.e: locally or during the entire manufacturing), may help to improve the properties of the part without post-elaboration heat treatments.

## 2. Material and experimental procedure

### 2.1. Material and Elaboration

This investigation was performed on Hastelloy X superalloys. This material is used in aeronautics applications for its good mechanical properties and corrosion resistance at elevated temperature [19–21]. Like other Ni-based superalloys, this material is suitable for additive manufacturing [22–25].

The precursor powder of this material was provided by Auber and Duval with powder particle average diameter around 30  $\mu\text{m}$ . The typical chemical composition of this alloy is reported in table 1.

Table 1: Typical chemical composition of the Hastelloy X alloy employed in this study.

C	Mn	P	S	Si	Cr	Mo	Co	Fe	W	Ni
0.05-0.15	1.0 max	0.04 max	0.03 max	1 max	20.5-23.0	8.0-10.0	0.5-2.5	17.0-20.0	0.2-1.0	bal.

The elaboration was performed on an EOS M290 powder bed fusion machine at ArianeGroup company. The basic parameters set employed for the elaboration is summarized in table 2. For the double laser scan strategy, for a given sample, the second scan starts immediately after the first one and follows the same path as the previous one. In order to investigate the role played by laser rescanning with different powers, six parameter sets were considered for the elaboration (see table 2): one reference Single-Laser Scan (LS) strategy (labelled - Ref. 1LS - in the following paragraphs) and 5 double-laser scan strategies with different laser powers during the second scan (referred to as - 2LSxx - in the text, where xx represents the % of 1st laser scan power during the second scan).

Table 2: Summary of the elaboration parameters for the Hastelloy X samples using powder bed fusion investigated in this study. 1LS: single laser scan, 2LS: double laser scan.

sample	1st laser power (W)	2nd laser power (W)	Laser speed (mm/s)	Hatch distance (mm)	Powder height ( $\mu\text{m}$ )	Scan angle ( $^\circ$ )	Total cumulated layer volumic energy ( $\text{J}/\text{mm}^3$ )
Ref. 1LS	285	-	960	0.11	40	67	67.5
2LS100		285					135
2LS80		228					121.5
2LS60	285	171	960	0.11	N.A.	N.A.	108
2LS40		114					94.5
2LS20		57					81

To investigate the microstructure and mechanical properties, 3 cylinders of 20 mm diameter and 90 mm height were manufactured for each parameter sets. Figure 1 illustrates the position of the cylinders on the elaboration plate. For the reference single-laser scan strategy, one sample was submitted to a solution Heat Treatment (H.T.) at 1175 ° C during 2 hours at air and then air cooled (H.T. similar to the one reported by Heynes data sheet) [26]. This sample is labelled Ref. 1LS H.T. in the following paragraphs.

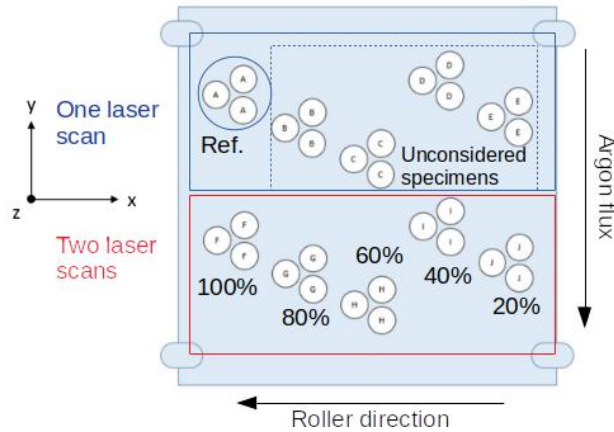


Figure 1: Illustration of sample distribution on the elaboration plate of the EOS M290 employed in this study. For each sample of the two laser scan strategies, the laser power on the second scan is expressed in % of the applied power during the first scan.

## 2.2. Mechanical characterization

In order to avoid typical A.M. surface roughness which may affect the mechanical properties, the cylinders were machined to obtain conventional tensile test specimens following the ISO 12126:2017 standards with a gauge length of 16 mm and a 8 mm diameter. One monotonic and two loading/unloading tensile tests were performed for each condition using an electromechanical MTS C45 tensile machine with a cross head displacement control. The axial strain was recorded by means of conventional "clip-on" extensometer. The applied strain rate was about  $5 \cdot 10^{-3} \text{ s}^{-1}$ .

Compared to monotonic tensile tests, loading/unloading tests enable us to investigate of the loading surface as a function of the axial strain. Using this loading surface, the flow stress can be divided into two components

named backstress and effective stress [27–29]. The backstress is then associated with the center of the loading surface whereas the effective stress is related to the radius of this surface as illustrated in figure 2. These two stress components are linked to different interactions of mobile dislocations with the microstructure. The effective stress corresponds to short range ones such as forest dislocation interactions or small coherent precipitates with dislocations. Backstress is related to long range interactions between mobile dislocations and strong defects like heterogeneous dislocation structures, incoherent precipitates or grain boundaries. The knowledge of the evolution of these stress components along with strain gives valuable information of the plasticity mechanisms. More details on the computation of these two stress components and their physical meaning can be found in other articles [27; 28].

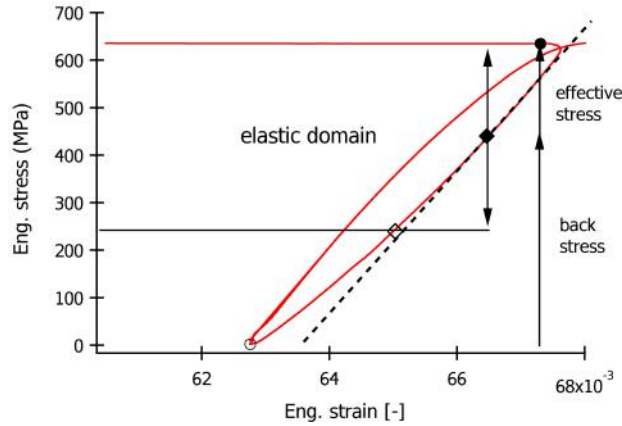


Figure 2: Illustration of the stress decomposition during one unload/load sequence applied to an A.M. Hastelloy X sample.

### 2.3. Material and microstructural characterization

To understand the origin of this change in mechanical properties resulting from the different elaboration parameter sets, microstructural characterization was performed. First, density was measured for each elaboration conditions using an Archimedes type balance (precision measurement of 0.1 g) and a 5 mm high sample extracted at the top of the manufactured cylinders. 10 measurements were recorded for each sample and the average value along with the statistical error with a confidence index of 95% were computed.

Second Scanning Electron Microscope (SEM - JEOL 7900F) coupled Secondary Electrons (SE), BackScattered Electrons (BSE) and Electron BackScattered Diffraction (EBSD) were employed to investigate the melting pools and dendrites, the fracture surfaces, the grain sizes, the crystallographic texture, the precipitates and dislocation structures. These features were analysed in three planes: x-y, x-z and y-z, these three directions corresponding to the elaboration plate (see figure 1). For these analysis, samples were mechanically polished up to a 1200 SiC paper. A final step of electropolishing using A2 Struers electrolyte (20 V - 30 s) was systematically applied prior to the observations. For melting pool analysis, this electropolishing step was followed by an electrochemical attack at 10 V during approximately 3 s. For EBSD, the sample observations were performed with a high voltage of 25 kV and with a electron current of 5 nA. Same scan area dimensions (800 x 600  $\mu\text{m}$ ) and step (0.7  $\mu\text{m}$ ) were employed for each sample. For dislocation imaging, Electron Channeling Contrast Imaging (ECCI) was performed using BSE detector with the following SEM conditions: 25kV of high voltage, 5 nA current and about 6 mm for the working distance.

### 3. Results

#### 3.1. Initial material characterization

Figure 3 illustrates the Melting Pools (M.P.) in the plane y-z observed by scanning electron microscope (secondary electrons) for the reference parameters set (Ref. 1LS) in fig. 3(a), the 2LS100 conditions in fig. 3(b), the 2LS80 conditions in fig. 3(c) and the 2LS60 conditions in fig. 3(d).

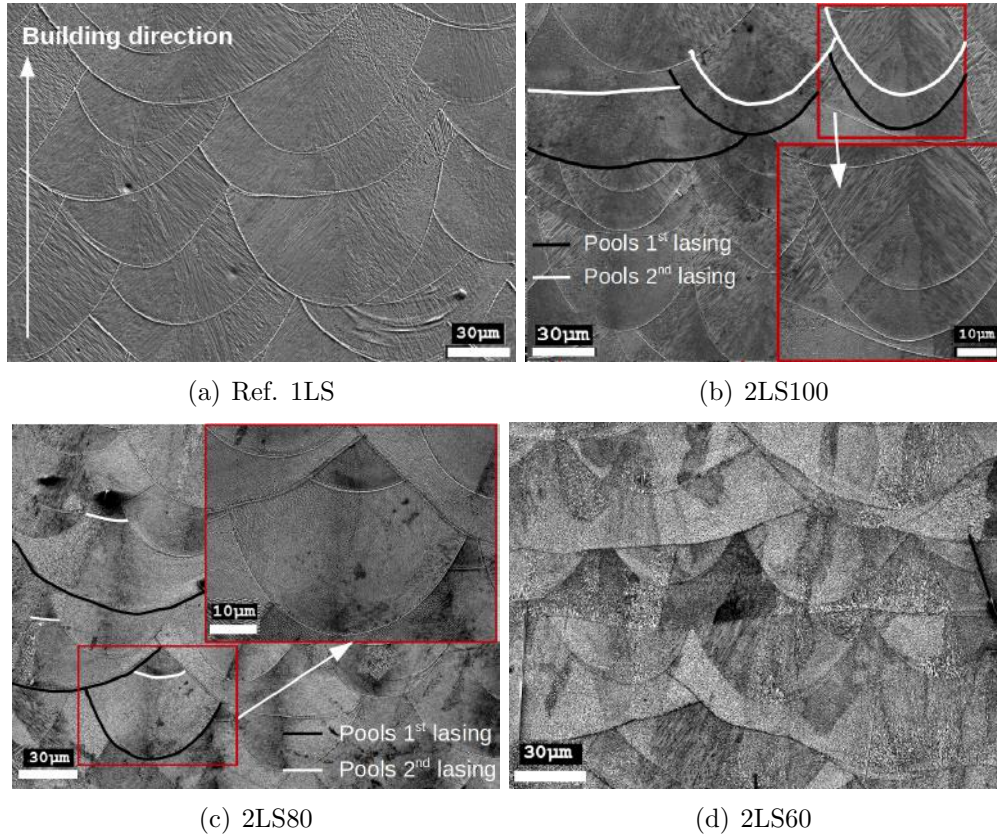


Figure 3: SEM analyses of the melting pools for: (a) the reference single-laser scanned sample (Ref. 1LS), (b) the double-laser scanned sample at 100% laser power (2LS100), (c) the double laser scanned sample at 80% laser power (2LS80) and (d) the double laser scanned sample at 60% laser power (2LS60). Building direction is vertical.

For the reference conditions (fig. 3(a)), conventional pools are observed. Their width dimensions correspond to the hatch distance. For the two conditions with laser rescanning at 100% and 80% powers, observed in fig. 3(b) and in fig. 3(c), changes in the melting pools are observed compared to the reference conditions.

With a full power laser rescan (2LS100), two different pools can be observed as schematically indicated in fig. 3(b). The first M.P. boundary, illustrated by a black solid line, represents the extend of the melting during the first scan. The second one, represented with a white solid line, illustrates the M.P. boundary of the second scan. For instance, the zoom inserted in the figure highlights an example of these two kinds of melting pools. Due to the larger thermal conductivity of solid material compared to powders [30; 31], remelting during the second laser scan is only partial. With a decrease in second scan laser power, the depth difference between the first and second scan M.P. increased as illustrated in fig. 3(c). For 2LS60 samples, no remelting is observed in fig. 3(d). The same observations can be made for 2LS40 and 2LS20 samples (not shown here).

To better characterize the microstructural modifications resulting from the 2LS conditions, the morphological and crystallographical texture were investigated by EBSD on all samples. The analysis were performed on the three observation planes, x-y, x-z and y-z. For the reference sample (Ref. 1LS), the laser direction is clearly visible in the x-y plane (fig. 4(a)). In this plane, grains are rectangular in shape with an elongation perpendicular to the laser direction with a dominance of the [011] orientation along the normal of the plane (z-building direction). Small equiaxed grains are also observed between each laser track. On the x-z and y-z planes, illustrated fig. 4(b) and fig. 4(c) respectively, elongated grains aligned with the building direction are observed with strong preferential crystal orientation. For these three observation planes, the corresponding pole figures are plotted fig. 5(a) (x-y plane), fig. 5(b) (x-z plane) and fig. 5(c) (y-z plane). As observed in the grain orientation maps, strong crystallographical textures with maximal density poles larger than 10 M.R.D. (for Multiple Random Distribution) are revealed for this reference sample. In the x-z plane (figure 5(b)), a Goss texture  $\{110\} \langle 001 \rangle$  is observed. In the y-z plane (figure 5(c)), the same  $\{110\} \langle 001 \rangle$  texture is also characterized. It is worth noticing that pole figures illustrated in figure 5(b) and figure 5(c) are given in different sample

coordinates. However, the preferential grain orientations correspond to a single texture component if similar sample coordinates are employed for both pole figures. This Goss texture component has been already characterized for Ni-alloys obtained by additive manufacturing [32; 33] and steels [34; 35] and is related to the specific heat flux direction and associated solidification in A.M. [32; 34].

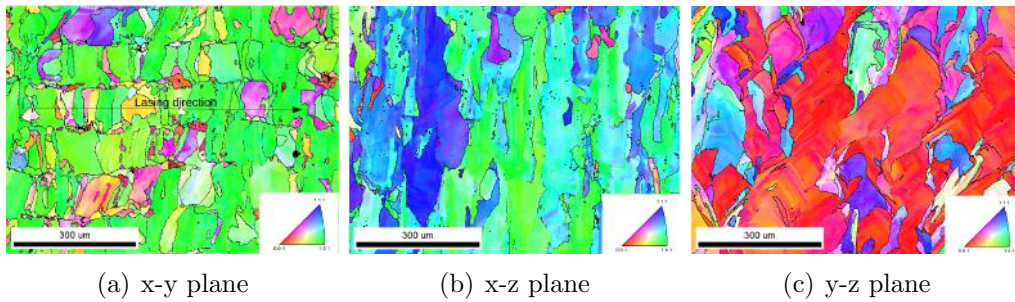


Figure 4: Grain orientation maps for the reference single laser scan sample - 1LS - for the three planes: (a) x-y, (b) x-z and (c) y-z. See figure 1 for the illustration of the axis with respect to the elaboration plate. Standard triangle is given with respect to the normal direction. For (b) and (c), building direction is vertical.

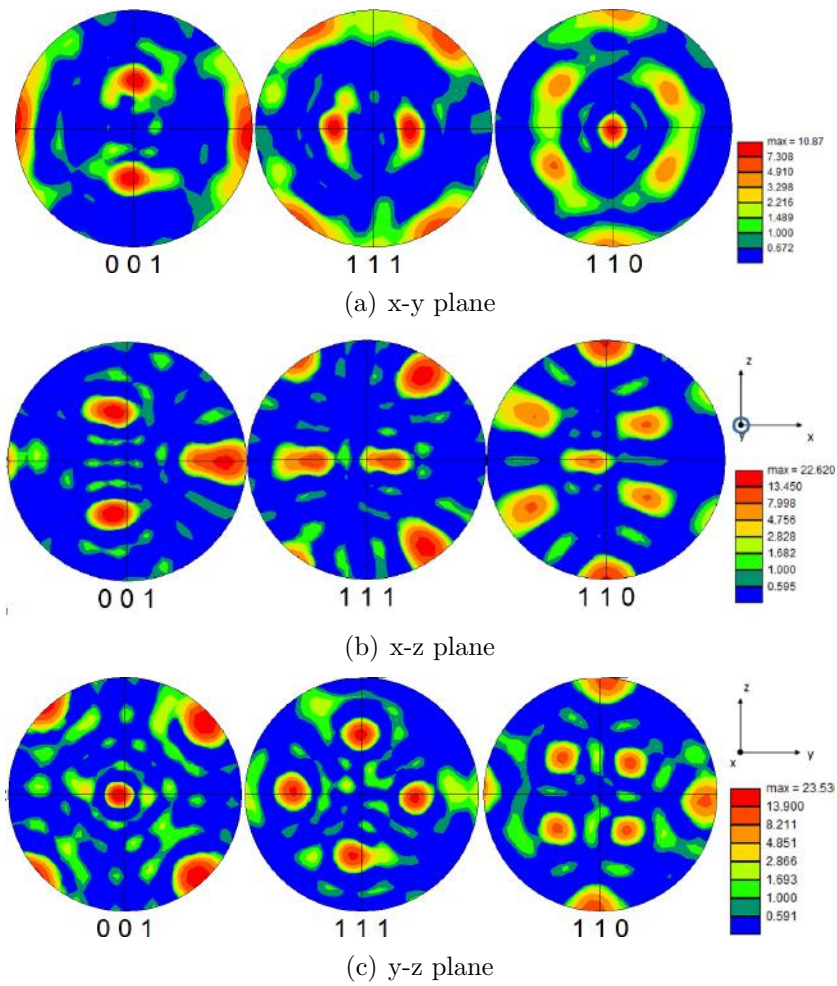


Figure 5: Pole figures of the crystallographic planes (001), (111) and (011) of the reference sample with one laser scan (1LS) for the planes: (a) x-y, (b) x-z and (c) y-z. See figure 1 for the illustration of the axis with respect to the elaboration plate.

Figure 6 illustrates the grain orientation maps on the three planes x-y, x-z and y-z for the 2LS100 (fig. 6(a) to fig. 6(c)), the 2LS60 (fig. 6(d) to fig. 6(f)) and 2LS20 (fig. 6(g) to fig. 6(i)). Compared to the reference 1LS sample, similar grain orientations are observed in the three planes for the three double laser scan conditions (2LS100, 2LS60 and 2LS20), revealing a similar Goss texture.

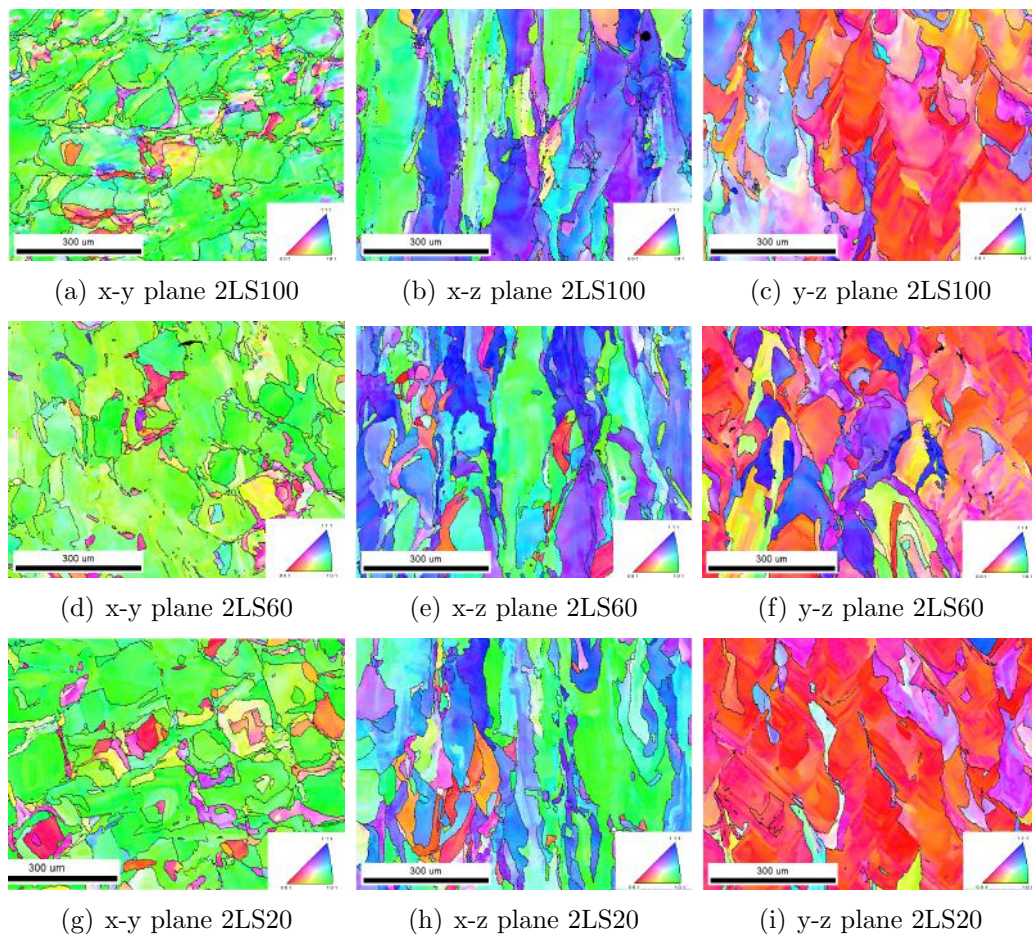


Figure 6: Grain orientation maps for the double laser scanned samples with 100%, 60% and 20% of laser power. Observation planes are indicated in the subcaptions of the figure. See figure 1 for the illustration of the axis with respect to the elaboration plate. Standard triangle is given with respect to the normal direction of the observation plane.

Compared to the reference 1LS sample, as illustrated in figure 7(a) and in figure 7(b), a grain orientation spread can be observed in the y-z plane of the 2LS100 and 2LS60 samples with a decrease in the maximal density pole. For the third double laser scanned sample at 20% laser power, no difference is observed compared to the reference 1LS sample with similar poles and corresponding densities.

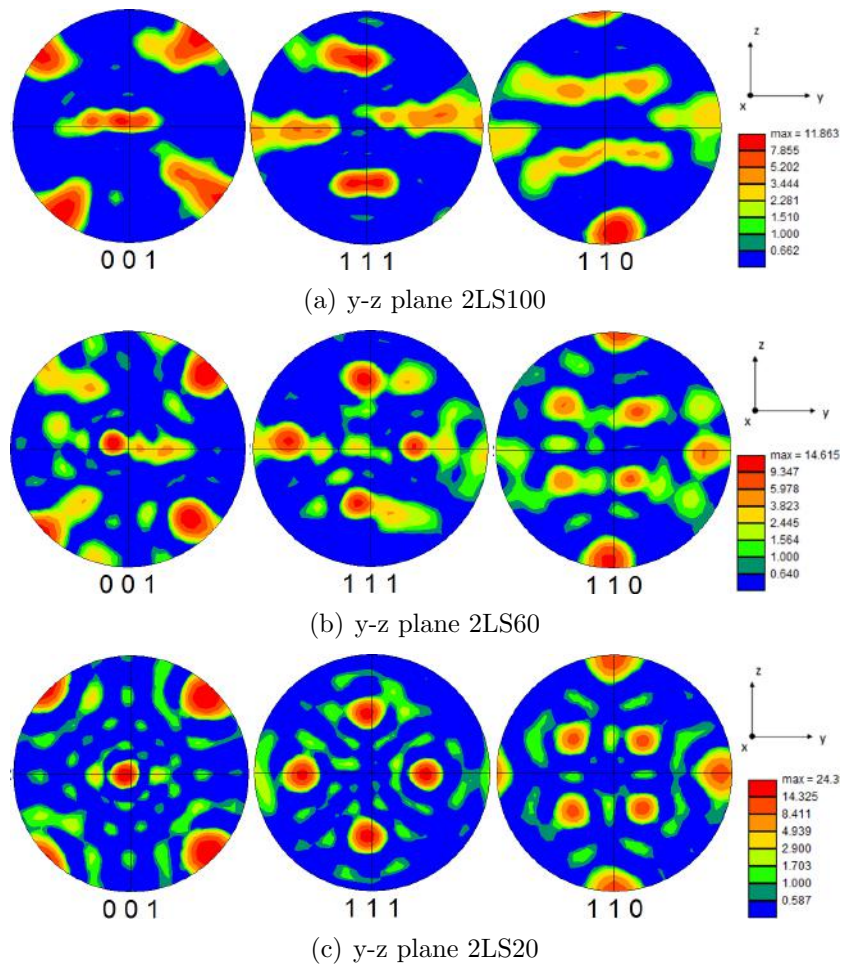
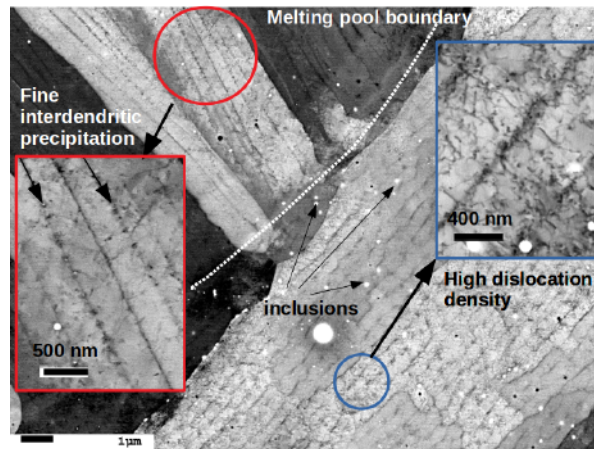


Figure 7: Pole figures of the crystallographic planes (001), (111) and (011) in the plane y-z for samples elaborated with the double laser scan conditions : (a) 100% laser power - 2LS100, (b) 60% laser power - 2LS60 and (c) 20% laser power - 2LS20. See figure 1 for the illustration of the axis with respect to the elaboration plate.

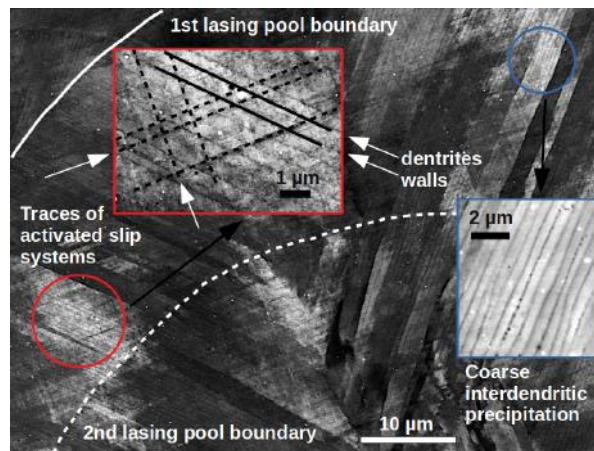
Figure 8 illustrates the microstructure observed by SEM using backscattered electrons of the reference 1LS sample (fig. 8(a)), the double laser scanned sample at 100% of power, 2LS100 (fig. 8(b)) and the double laser scanned sample at 60% power, 2LS60 (fig. 8(c)). These observations were carried out on the y-z plane with a sample tilt of  $0^\circ$  with respect to the electron axis. For each sample, several grains in various melting pools were observed in order to ensure that the differences in microstructure between the manufacturing conditions are statistically representative and may not result from a difference in grain orientation (not characterized for each observed area) which could change the dislocation contrast [36].

For the reference sample, firstly, heterogeneous dislocation structures are observed inside the grains. As illustrated in the blue inset of the figure 8(a), dislocations are mainly distributed in the interdendritic spaces with some isolated dislocations inside these dendrites. These dislocations appear as straight segments revealing the planar glide character of this material [37; 38]. In this figure, inside the grains, some misorientations also appear together with inclusions. Secondly, a fine interdendritic precipitation is characterized in the interdendritic spaces as highlighted in the red inset. The rough diameter of the precipitates is lower than 100 nm. These observations are similar to those reported by Pourbabak et. al. [39] for the sample material manufactured using a slightly lower volumic energy.

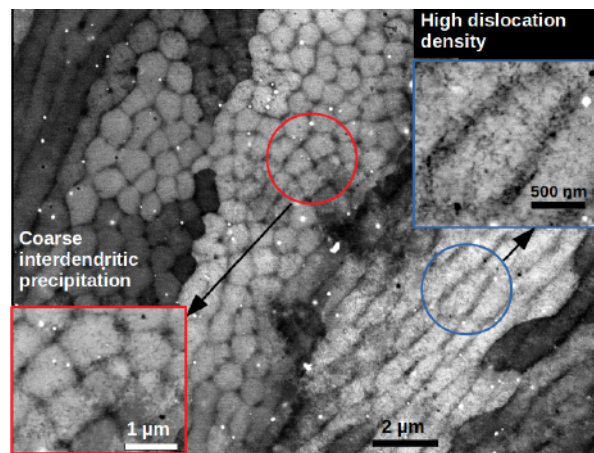
For the samples manufactured using the double laser scan conditions, the observations are similar to those of the reference sample. However, for the 2LS100 sample (fig. 8(b)), dislocation density seems to be higher than for the reference sample and several traces of activated slip systems are observed (see red inset), probably due to higher thermal stresses during the manufacturing process. The interdendritic precipitation also seems to be coarser (blue inset) compared to the reference sample. This coarse dendritic precipitation is also characterized for the 2LS60 sample as illustrated in figure 8(c) which does not exhibit various activated slip systems.



(a) 1LS



(b) 2LS100



(c) 2LS60

Figure 8: SEM observations using backscattered electrons of the microstructure of: (a) reference one laser scanned sample (Ref. 1LS), (b) 100% double laser scanned sample (2LS100) and (c) 60% double laser scanned sample (2LS60).

### 3.2. Mechanical properties assesment

Table 3 summarizes the volume mass computed using Archimedes method of all samples elaborated in this study. Taking into account the experimental errors on this measurement, all samples exhibit the same volume mass. The lasing strategy has, hence, no effect on this parameter.

Table 3: Volume mass measured by Archimedes balance of the Hastelloy X samples elaborated in this study. Corresponding experimental errors are computed with a confidence index of 95%.

Sample	Ref. 1LS	2LS100	2LS80	2LS60	2LS40	2LS20
Volume	8.347	8.344	8.325	8.329	8.340	8.348
mass (g.cm <sup>-3</sup> )	± 0.008	± 0.013	± 0.012	± 0.016	± 0.019	± 0.009

Figure 9 illustrates the tensile curves for the six elaboration conditions without heat treatment. The tensile curve related to the reference condition followed by the 1175 °C heat treatment during 2h is also indicated in this graph. Excepted for the heat treated sample, the flow stress level is similar for all samples obtained by additive manufacturing. Nevertheless, as observed in the inset of this figure, which represents a zoom on the plastic part of the tensile curves, several differences appear between the different elaboration conditions. First of all, as already observed in the pole figures, the mechanical response in tension of the Ref. 1LS sample and the 2LS20 sample are very similar. Second of all, for higher laser power during the second scan, a decrease in strain hardening rate is observed. Finally, the sample manufactured with 60% power during the second scan exhibits lower flow stress and larger plastic strain at necking compare to other samples.

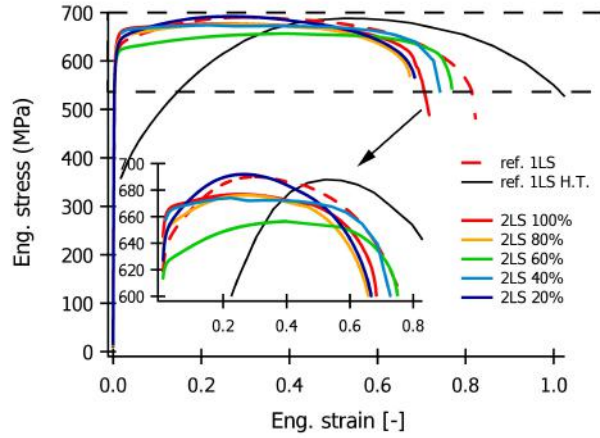


Figure 9: Engineering tensile curves of the different Hastelloy X samples elaborated by powder bed fusion using single laser scan (1LS) and double laser scan (2LS) strategies.

In order to better analyse the differences in mechanical properties resulting from the rescanning strategies, the evolution of the average value of the yield stress, maximal stress, necking and failure strains are plotted as a function of the elaboration conditions in fig. 10(a) for stresses and in fig. 10(b) for strains. These average values and corresponding error bars (10%) are computed using the monotonic and loading/unloading tests. The typical values of a solution heat treated (1175 °2 h air cooled) cast sample, provided by Heyne’s data sheet [26], are also indicated in these figures with horizontal lines.

With regard to the yield stress (figure 10(a)), a higher value of this parameter is observed for the rescanning strategy with full power (2LS100 sample). With a decrease in the laser power during the second laser scan, the yield stress tends to the value obtained in the reference 1LS conditions. All samples manufactured by AM without heat treatment exhibit values larger than the heat treated samples.

For the ultimate tensile strength, the larger values are obtained in the reference conditions and the rescanning with a laser power of 20%. The lower value is obtained for a rescanning with a power reduction of 40% (2LS60) whereas 2LS100, 2LS80 and 2LS40 exhibit intermediate values. Taking into account the experimental scattering indicated by the error bars, the differ-

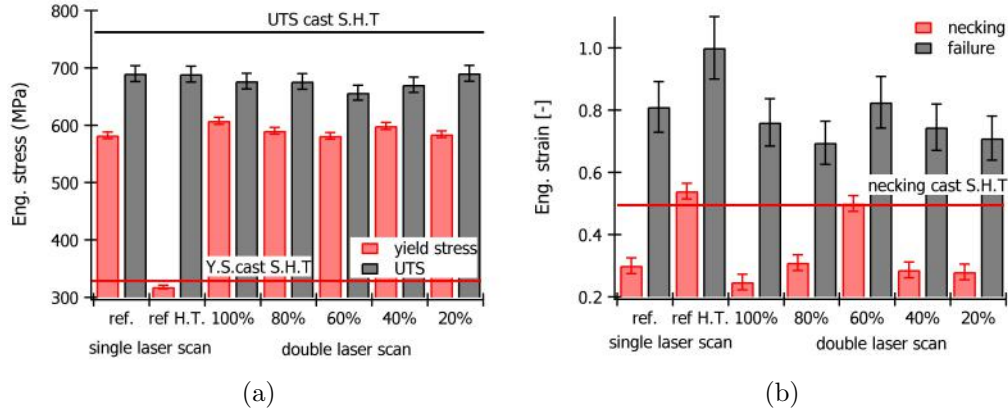


Figure 10: Influence of the elaboration conditions on (a) yield stress and ultimate tensile strength and (b) necking and fracture strains for Hastelloy X elaborated by powder bed fusion.

ences are, nevertheless, not statistically significant. It should be mentioned that all the values of P.B.F. samples remain lower of about 100 MPa than the expected one for a heat-treated cast samples.

As far the necking strain is concerned, the maximal value 0.5 is obtained in the 2LS60 conditions whereas other samples have similar values close to 0.3. This significant necking strain for the 2LS60 sample is similar to the one of the ref. 1LS H.T. samples and higher than values reported for the same alloy elaborated by P.B.F. (without rescanning) and heat treated in the same conditions [22] and also with HIP treatment [40]. This 0.5 necking strain characterized for the 2LS60 sample is, moreover, similar to the value reported for a H.T. cast sample [26]. For strain at failure, taking into account the experimental scattering, the elaboration conditions do not seem to affect this property for Hastelloy X samples elaborated by P.B.F. and subjected to mechanical loading in the building direction.

These changes in the mechanical properties resulting from the elaboration conditions are also observed in the evolution of the backstress and the effective stress obtained from the loading/unloading tests. Figure 11(a) illustrates the evolution of the effective stress as a function of strain for the different samples. Regardless the elaboration conditions, this flow stress component is reduced with an increase in strain up to 0.1. For higher strain

values, the effective stress is constant. The reference sample exhibits slightly larger values than those of the samples obtained with the rescanning strategy which do not seem to depend on the power of the second laser scan, except for the 2LS20 with similar values as Ref. 1LS sample. Compared to the heat treated sample, all the AM samples have higher effective stress values (difference lower than 50 MPa) for strain lower than 0.4. Due to its strain hardening capacity resulting from recrystallization, the effective stress of the H.T. sample strongly increases along with large strains to reach similar values as in other samples.

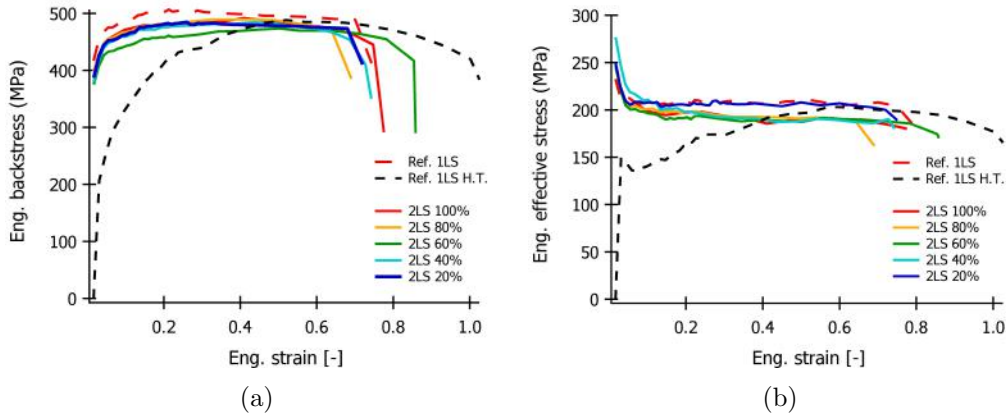
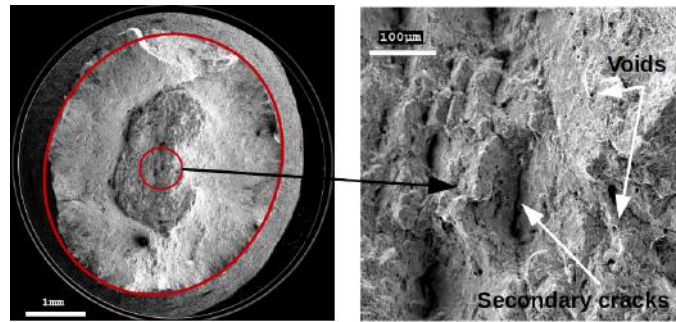


Figure 11: Influence of elaboration conditions on the engineering backstress (a) and effective stress (b).

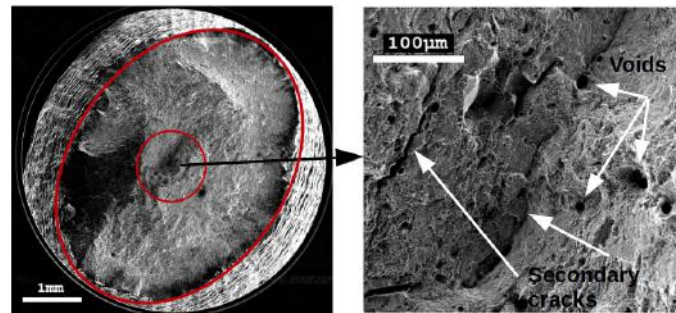
The evolution of the backstress along with strain is also similar for all samples. Nevertheless, contrary to the effective stress, an increase in strain results in an increase in backstress. The backstress level weakly depends on the elaboration conditions as similar values are obtained for all samples. However, the 2LS60 sample exhibits the lowest value. Similarly to the effective stress, the backstress of the heat treated sample is about 200 MPa lower than the A.M. samples at the onset of plasticity. With an increase in plastic strain, backstress difference between all samples tends to be reduced. These results suggest that the higher flow stresses of A.M. samples compared to casted ones are clearly correlated to the backstress component.

After sample failure, fracture surfaces were observed by SEM. Figure 12

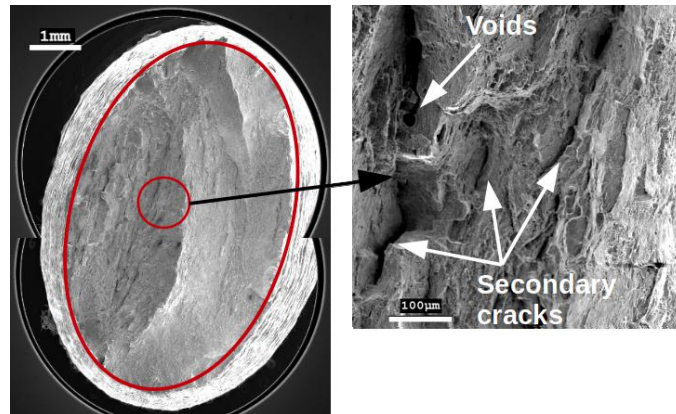
represents these fracture surfaces for four elaboration conditions: 1LS reference with heat treatment (Ref. 1LS H.T. - fig. 12(a)), 1LS reference without heat treatment (Ref. 1LS - fig. 12(b)), 2LS100 (fig. 12(c)) and 2LS60 (fig. 12(d)). For all conditions, ductile fracture is revealed by dimples in agreement with the large fracture strain observed in figure 10(b). For the heat treated conditions, the conventional cup and cone surface is observed with void nucleation, growth and coalescence in the center part of the sample and shear fracture near the surface. For the three other conditions these cups and cones fractures are not observed. Fracture seem, hence, to be dominated by shear. Moreover, for these latter conditions without H.T., voids are observed and the sample section is not longer circular. Elliptical shape is observed which is more pronounced for the double laser scanned samples (fig. 12(c) and fig. 12(d)). These non circular fracture surfaces suggest a important plastic anisotropy associated with the strong crystallographic texture. Secondary cracks aligned with the larger dimension of the cross section are also observed in these samples.



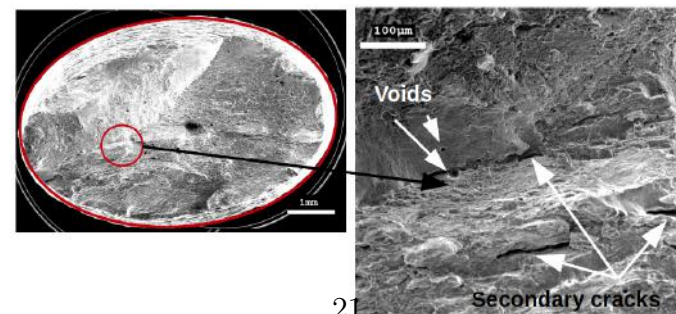
(a) ref. 1LS H.T.



(b) ref. 1LS



(c) 2LS100



(d) 2LS60

Figure 12: Scanning electron microscope observations of the fracture surfaces for four Hastelloy X samples analysed in this study: (a) heat treated, (b) reference single laser scanned conditions, (c) double laser scanned with 100% power and (d) double laser scanned with 60% power.

## 4. Discussion

All results presented in the previous sections show a significant effect of the rescanning strategy on both microstructures and mechanical properties. These changes are discussed in the following paragraphs in terms of remelting, crystallographical and morphological texture, backstress and laser power.

### 4.1. Microstructure and thermal history modifications

As observed in the previous paragraphs, the elaboration conditions influence the microstructure of the sample. The melting pools, the morphological texture or dominant grain orientations are dependent on these conditions.

Table 4 summarizes the different microstructural characteristics, grain size, grain circularity, and the maximal density pole for the Goss texture component for five samples: Ref. 1LS H.T., Ref. 1LS, 2LS100, 2LS60 and 2LS20. These three double laser conditions correspond to: deep remelting, no remelting with best mechanical properties, no remelting with mechanical properties close to the reference sample, respectively. The grain size was computed using the average area converted then into diameter assuming, at first approximation, spherical grains. In addition, this value was obtained considering an average value based on each plane one (no huge difference was found between each plane). For the heat treated reference sample, full recrystallization occurred leading to an isotropic texture with a low maximal density pole (6 MRD) ensuring no plastic anisotropy.

Table 4: Summary of some microstructural characteristics (grain size, grain circularity and maximal density pole -  $I_{max}$ ) of the Hastelloy X samples investigated in this study. Grain size and circularity values are given with a relative error bar of 50%.

sample	grain size ( $\mu\text{m}$ )	grain circularity	$I_{max}$ (m.r.d.)
Ref. 1LS H.T.	22	0.36	N/A
Ref. 1LS	18	0.39	20
2LS100	19	0.40	15
2LS60	20	0.41	17
2LS20	28	0.35	20

Based on the analyses of these data, it appears that the rescanning strategy does not affect the grain size and grain circularity as very similar values are obtained for all samples. Grain size is, hence, not the relevant length scale

to understand the dependence of mechanical properties with the lasing strategy. For the texture analysis, except for the heat treated sample, the strong Goss texture component reveals no strong modification of solidification during the process. Nevertheless, as already suggested by the comparison of the pole figures for the Ref. 1LS (fig. 5) and 2LS conditions (fig. 7), revealing a spread of the preferential grain orientations for the 2LS100 and 2LS60 sample, these two samples exhibit a slight reduction in the maximal density pole for the Goss texture component. In order to highlight this feature, a analysis of the grain orientation distribution with respect to the dominant  $\{110\}$  plane normal aligned with the Z sample direction was considered. Figure 13 illustrates the cumulative grain number fraction as a function of the crystal orientation.

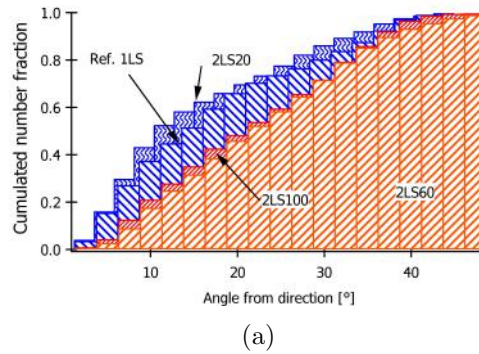


Figure 13: Cumulative grain number fraction as a function of the crystal misorientation with respect to the theoretical Goss texture.

As illustrated in this figure, compared to the reference sample, the spread of preferential grain orientations for the 2LS100 and 2LS60 samples is clearly evidenced. For these two samples, the number fraction of grains oriented within  $20^\circ$  with respect to the theoretical crystal direction is about 40% vs 60% for the reference sample. Considering the relationship between the process, i.e., directional solidification, it seems that the second lasing strategy affects the solidification. For the 2LS20 sample, with a second laser scan power about 20% of the first one, the grain orientation distribution is very close to the reference sample.

In f.c.c. and some b.c.c. materials, solidification occurs with the  $\langle 001 \rangle$

direction aligned with the heat flux or thermal gradient [41]. For additive manufacturing processes, this feature may lead to a strong Goss texture with the  $\langle 011 \rangle$  aligned with the building direction if no laser scanning rotation is applied between each layer [42]. In this case, dendrite growth will occur following the maximal thermal gradient which is oriented at  $45^\circ$  with the building direction. When a scanning rotation is applied, the thermal gradient direction will change from a layer to another and a competition will take place between the nucleation and growth of new dendrites aligned with the thermal gradient, and the epitaxial dendrite growth from the former solidified ones (in the previous layer or in the same one). From this competition, significant misorientations are observed inside the grains giving rise to the so-called chevron patterns [34]. Moreover, different crystallographical and morphological texture may appear depending on the scanning strategy [43].

Despite the  $67^\circ$  laser scanning rotation between each layer, the strong Goss texture in the ref. 1LS and 2LS20 samples suggests that, for these two samples, epitaxial growth is the main solidification mechanism. However, as observed in figure 4 and in figure 6(c), for the Ref. 1LS and 2LS20 samples respectively, the chevron patterns indicate that dendrite nucleation also takes place during solidification.

For the 2LS100 and 2LS60 conditions, despite a similar laser scanning strategy, the reduction in the well oriented grain volume fraction with respect to the theoretical Goss texture, reveals that the the solidification process is affected. During the process, due to the double laser scan strategy, the temperature of these samples will be larger than the one for the reference conditions for which the sample can cool down between each laser scanning. Consequently, the thermal gradient or heat flux will be lower if the laser power during the second scan is high enough. Following the conclusions drawn by Andreau et. al. [34], this decrease in thermal gradient will enhance epitaxial grain growth as the driving force for nucleation is lower. This feature, first, will reduce the dominant  $\langle 011 \rangle$  crystal direction parallel with the building direction as observed in figure 13. Second, it will also reduce the chevron pattern as observed qualitatively in figure 6(a) and figure 6(b) compare to the reference sample (see fig.4).

This increase in temperature for the high energy double laser scanned samples, involving the modification of the thermal gradient may also induce

a modification in the cooling rate compared to the reference conditions. As already reported in literature, for IN718 Ni-superalloys, the cooling rate ( $\dot{T}$ ) is related to the dendrite size ( $\lambda$ ) following equation 1 [44]:

$$\lambda = 97\dot{T}^{-0.36} \quad (1)$$

An image analysis of the dendrite size was performed on the SEM observations carried out in the y-z plane for the Ref. 1LS, 2LS100 and 2LS60 conditions. Average values of  $\lambda$ , based on 8 images taken from different melting pools, are summarized in table 5.

Table 5: Dendrite space measurements and corresponding estimation of the cooling rate for the reference conditions and double lasing conditions with 100% and 60% nominal laser power. Error bars are given with a confidence index of 95%.

sample	dendrite size ( $\mu m$ )	cooling rate ( $K.s^{-1}$ )
Ref. 1LS	$0.46 \pm 0.08$	$(2.86 \pm 0.18) 10^6$
2LS60	$0.42 \pm 0.09$	$(3.68 \pm 0.29) 10^6$
2LS100	$0.33 \pm 0.04$	$(7.2 \pm 0.34) 10^6$

The comparison of the cooling rate values for the reference and 2LS60 conditions (which does not induce remelting) reveals that, due to the increase in temperature related to the second laser scan, the cooling rate is slightly increased for this double laser scan sample. When it comes to the 2LS100 samples, for which large remelting occurs, the cooling rate was increased by a factor 2.5 compared to the reference sample. For this sample, remelting occurs on a full solidified layer. Due to the increase in thermal conductivity for solids compared to powders [30; 31] this remelting leads to larger cooling rates which strongly influence the dendritic space. This increase in  $\dot{T}$  can explain, hence, the activation various slip systems during the cooling down of the 2LS100 samples, as illustrated in figure 8(b).

#### 4.2. Effect on the mechanical properties

The microstructural modifications due to the relationship between the manufacturing strategy and the thermal history are expected play a role on the mechanical properties.

As observed in figure 10(a), the yield stress is dependent on the scanning strategy. As the grain size is virtually the same for all samples (see table 4), the yield stress is not related to this parameter. The differences in dendrite size characterized in the previous section between Ref. 1LS, 2LS100 and 2LS60 samples may explain this modifications in yield stress. 2LS100 sample exhibits the larger yield stress (607 MPa) and lower dendrite size ( $0.33 \mu\text{m}$ ) compared to the two other samples with similar values of yield stress (581 and 582 MPa for Ref. 1LS. and 2LS60 samples, respectively) and dendrite size ( $0.46 \mu\text{m}$  - Ref. 1LS vs  $0.42 \mu\text{m}$  - 2LS60). In plasticity, the dendrite walls will act as strong dislocation barriers which involve, in turn, an increase in yield stress following the well known Hall-Petch relationship [45–47].

However, despite a similar initial dendrite size value and yield stress, the Ref. 1LS and 2LS60 samples exhibit different strain hardening involving different flow stress level during plasticity (see figure 9). The evolution of the effective stress and backstress for the different samples considered in this study (figure 11) reveal that both stress components are affected by the elaboration strategy and can help to understand the effect of the second lasing.

For the effective stress, related to short range interactions between mobile dislocations and the microstructure, the higher values for the Ref. 1LS and 2LS20 suggest that the slight differences in dislocation density or precipitation, characterized in figure 8, play a role on the mechanical properties. These defects will participate to the dislocation anchorage which will increase the strain hardening [28; 48] as observed in figure 9. This increase in strain hardening will, in turn, lead to larger flow stress during plasticity for the Ref. 1LS and 2LS20 compared to the 2LS60 sample despite a similar initial dendrite size.

For the backstress, this stress component can be divided into two parts, a intragranular corresponding to the formation of heterogeneous dislocation structures and, a intergranular one, related to the strain incompatibilities between grains (grain size effect) [27; 28]. As the grain size is virtually the same for all samples, the backstress is expected to be related to the intragranular component only. Following a previous work on pure nickel, the intragranular backstress is inversely proportional to the dislocation cell size [49]. Taking into account this empirical relationship, according to the initial dendrite size of the Ref. 1LS, 2LS100 and 2LS60 samples, a larger value of backstress at

the beginning of plasticity is expected for the 2LS100 samples compared to the two other specimens. However, this feature is not characterized experimentally as illustrated in figure 11(a) and consequently, other mechanisms must be responsible for the larger backstress for the reference 1LS sample.

The grain orientation scattering with respect to the Goss texture for the 2LS100 and 2LS60 samples may first have modified the average Schmid factor and may lead to the activation, locally, of different slip systems. Second, the qualitatively larger density of chevron patterns associated with Geometrically Necessary Dislocations (G.N.D.) [34] for the single laser scan strategy may also contribute to the larger backstress value for the Ref. 1LS sample compared to the 2LS100 and 2LS60 ones.

Finally the different microstructural modifications can also explain the larger necking strain for the 2LS60 samples. Necking phenomena is associated with the dislocation storage capacity (strain hardening rate). Materials characterized by a low strain hardening rate generally exhibit low necking strain as observed for instance for ultrafine grained or nanocrystalline materials [50; 51]. Due to its lowest dendrite size which reduces the probability of dislocation storage, the 2LS100 sample is characterized by the lowest strain hardening rate (fig. 9) and consequently to the lowest necking strain as observed experimentally (see fig. 10(b)). For the Ref. 1LS and 2LS60 samples, the larger value of the initial dendrite size compared to the 2LS100 enhances the strain hardening rate and, in turn, the necking strain. This improvement is, however, lower for the Ref. 1LS specimen. This feature could be due to the increase in strain hardening associated to due to the larger density of dislocations as explained in the previous paragraphs. Hence, compared to the 2LS60 samples, the dislocation storage capacity, for the reference 1LS specimen, is reached at lower strain such as necking. It is assumed that the improved mechanical properties of the 2LS60 are then due to a good compromise between yield stress and strain hardening capacity resulting from the microstructural modifications above associated with the second lasing condition with intermediate laser power.

Transmission electron microscopy should be conducted to quantitatively investigate the differences in microstructure between the different lasing strategies to be able to quantify the contribution of each microstructural modification (i.e. dislocation, G.N.D., precipitation, texture . . . ), associated with

the second lasing strategy, on the mechanical properties.

## 5. Conclusions

In this study, the influence of a lasing strategy, with a systematic second lasing with different power, was investigated on the microstructure and mechanical properties of a Hastelloy X material elaborated by powder bed fusion processes. The main conclusions can be listed as follows:

1. the second lasing involves a partial remelting of the material resulting in two different melting pools if the power of the second scan is larger than 80% of the nominal power;
2. for high secondary lasing powers, the thermal gradient and cooling rates are modified leading to finer dendrites and lower Goss texture intensity;
3. the mechanical behavior is also affected by the double laser scan with a modification in strain hardening rate and an increase in ductility characterized by the necking strain;
4. the optimum mechanical properties (considering the processing conditions) are obtained for a second scan with a 60% power with a ductility similar to the one of a heat treated samples but with a yield stress increased by a factor 2.5;
5. a significant plastic anisotropy is observed for all samples characterized as-received due to the strong crystallographic texture.

Finally, this lasing strategy could be considered to manufacture high damage resistance material (high yield stress and necking plastic strain) taking advantage of the additive manufacturing processes without heat treatment. Further characterization of the microstructure and numerical simulations are nevertheless required to better understand the role played by the double laser scan strategy on the mechanical properties.

## 6. Acknowledgments

The Normandy Region and European Union (European Regional Development Fund) are greatly acknowledged for the financial support of the CLIP FAM project.

## 7. Data availability

The raw/processed data required to reproduce these findings cannot be shared at this time as the data also forms part of an ongoing study.

## References

- [1] T. DebRoy, H. Wei, J. Zuback, T. Mukherjee, J. Elmer, J. Milewski, A. Beese, A. Wilson-Heid, A. De, W. Zhang, Additive manufacturing of metallic components process, structure and properties, *Progress in Materials Science* 92 (2018) 112 – 224.
- [2] J.-P. Kruth, M. Badrossamay, E. Yasa, J. Deckers, L. Thijs, J. Humbeeck, Part and material properties in selective laser melting of metals, 16th International Symposium on Electromachining, ISEM 2010 (01 2010).
- [3] B. Cheng, S. Shrestha, K. Chou, Stress and deformation evaluations of scanning strategy effect in selective laser melting, *Additive Manufacturing* 12 (2016) 240 – 251.
- [4] K. Guan, Z. Wang, M. Gao, X. Li, X. Zeng, Effects of processing parameters on tensile properties of selective laser melted 304 stainless steel, *Materials Design* 50 (2013) 581 – 586.
- [5] P. Hanzl, M. Zetek, T. Bakša, T. Kroupa, The influence of processing parameters on the mechanical properties of slm parts, *Procedia Engineering* 100 (1) (2015) 1405–1413.
- [6] J. Robinson, I. Ashton, P. Fox, E. Jones, C. Sutcliffe, Determination of the effect of scan strategy on residual stress in laser powder bed fusion additive manufacturing, *Additive Manufacturing* 23 (2018) 13 – 24.

- [7] H. Taheri, M. Shoaib, L. W. Koester, T. A. Bigelow, P. C. Collins, L. J. Bond, Powder based additive manufacturing-a review of types of defects, generation mechanisms, detection, property evaluation and metrology, *Int. J. Addit. Subtractive Mater. Manuf* 1 (2) (2017) 172–209.
- [8] M. Shiomi, K. Osakada, K. Nakamura, T. Yamashita, F. Abe, Residual stress within metallic model made by selective laser melting process, *CIRP Annals* 53 (1) (2004) 195 – 198.
- [9] J.-P. Kruth, J. Deckers, E. Yasa, R. Wauthl, Assessing and comparing influencing factors of residual stresses in selective laser melting using a novel analysis method, *Proceedings of the Institution of Mechanical Engineers, Part B: Journal of Engineering Manufacture* 226 (6) (2012) 980–991.
- [10] P. Mercelis, J. Kruth, Residual stresses in selective laser sintering and selective laser melting, *Rapid Prototyping Journal* 12 (5) (2006) 254–265.
- [11] H. Ali, H. Ghadbeigi, K. Mumtaz, Effect of scanning strategies on residual stress and mechanical properties of selective laser melted ti6al4v, *Materials Science and Engineering: A* 712 (2018) 175 – 187.
- [12] K. Wei, M. Lv, X. Zeng, Z. Xiao, G. Huang, M. Liu, J. Deng, Effect of laser remelting on deposition quality, residual stress, microstructure, and mechanical property of selective laser melting processed ti-5al-2.5sn alloy, *Materials Characterization* 150 (2019) 67 – 77.
- [13] E. Yasa, J. Deckers, J.-P. Kruth, The investigation of the influence of laser re-melting on density, surface quality and microstructure of selective laser melting parts, *Rapid Prototyping Journal* 17 (5) (2011) 312–327.
- [14] W. Yu, S. L. Sing, C. K. Chua, X. Tian, Influence of re-melting on surface roughness and porosity of alsil0mg parts fabricated by selective laser melting, *Journal of Alloys and Compounds* 792 (2019) 574 – 581.
- [15] Y. Tian, W. S. Gora, A. P. Cabo, L. L. Parimi, D. P. Hand, S. Tammas-Williams, P. B. Prangnell, Material interactions in laser polishing powder bed additive manufactured ti6al4v components, *Additive Manufacturing* 20 (2018) 11 – 22.

- [16] B. Liu, B.-Q. Li, Z. Li, Selective laser remelting of an additive layer manufacturing process on alsi10mg, *Results in Physics* 12 (2019) 982 – 988.
- [17] Z. Xiao, C. Chen, Z. Hu, H. Zhu, X. Zeng, Effect of rescanning cycles on the characteristics of selective laser melting of ti6al4v, *Optics Laser Technology* 122 (2020) 105890.
- [18] S. Griffiths, M. Rossell, J. Croteau, N. Vo, D. C. Dunand, C. Leinenbach, Effect of laser rescanning on the grain microstructure of a selective laser melted al-mg-zr alloy, *Materials Characterization* 143 (2018) 34–42.
- [19] Application of Hastelloy X in Gas-Cooled Reactor Systems, Standard, European Committee for Standardization (1976).
- [20] J.-W. Lee, Y.-C. Kuo, A study on the microstructure and cyclic oxidation behavior of the pack aluminized hastelloy x at 1100 c, *Surface and Coatings Technology* 201 (7) (2006) 3867 – 3871, proceedings of the 33rd International Conference on Metallurgical Coatings and Thin Films.
- [21] J.-C. Zhao, M. Larsen, V. Ravikumar, Phase precipitation and timetemperature-transformation diagram of hastelloy x, *Materials Science and Engineering: A* 293 (1) (2000) 112 – 119.
- [22] D. Tomus, Y. Tian, P. A. Rometsch, M. Heilmaier, X. Wu, Influence of post heat treatments on anisotropy of mechanical behaviour and microstructure of hastelloy-x parts produced by selective laser melting, *Materials Science and Engineering: A* 667 (2016) 42 – 53.
- [23] T. Etter, K. Kunze, F. Geiger, H. Meidani, Reduction in mechanical anisotropy through high temperature heat treatment of hastelloy x processed by selective laser melting (SLM), *IOP Conference Series: Materials Science and Engineering* 82 (2015) 012097.
- [24] Q. Han, R. Mertens, M. L. Montero-Sistiaga, S. Yang, R. Setchi, K. Vanmeensel, B. V. Hooreweder, S. L. Evans, H. Fan, Laser powder bed fusion of hastelloy x: Effects of hot isostatic pressing and the hot cracking mechanism, *Materials Science and Engineering: A* 732 (2018) 228 – 239.

- [25] D. Tomus, P. A. Rometsch, M. Heilmaier, X. Wu, Effect of minor alloying elements on crack-formation characteristics of hastelloy-x manufactured by selective laser melting, *Additive Manufacturing* 16 (2017) 65 – 72.
- [26] Hastelloy x alloy, <https://www.haynesintl.com/alloys/alloy-portfolio/High-temperature> accessed: 2020-01-30.
- [27] X. Feaugas, H. Haddou, Grain-size effects on tensile behaviour of nickel, AISI 316L stainless steel, *Metallurgical Transactions* 34A (2003) 2329 – 2340.
- [28] C. Keller, E. Hug, X. Feaugas, Microstructural size effects on mechanical properties of high purity nickel, *International Journal of Plasticity* 27 (4) (2011) 635 – 654.
- [29] J. Dickson, J. Boutin, L. Handfield, A comparaisn of two simple methods for measuring cyclic internal, effective stresses, *Material Science, Engineering* 64 (1984) L7 – L11.
- [30] S. Zhang, B. Lane, J. Whiting, K. Chou, On thermal properties of metallic powder in laser powder bed fusion additive manufacturing, *Journal of Manufacturing Processes* 47 (2019) 382 – 392.
- [31] J. Romano, L. Ladani, M. Sadowski, Thermal modeling of laser based additive manufacturing processes within common materials, *Procedia Manufacturing* 1 (2015) 238–250. doi:10.1016/j.promfg.2015.09.012.
- [32] D. Ma, A. D. Stoica, Z. Wang, A. M. Beese, Crystallographic texture in an additively manufactured nickel-base superalloy, *Materials Science and Engineering: A* 684 (2017) 47 – 53.
- [33] L. Dessieux, A. Stoica, P. Bingham, K. An, M. Frost, H. Bilheux, Neutron transmission simulation of texture in polycrystalline materials, *Nuclear Instruments and Methods in Physics Research Section B: Beam Interactions with Materials and Atoms* 459 (2019) 166 – 178.
- [34] O. Andreau, I. Koutiri, P. Peyre, J.-D. Penot, N. Saintier, E. Pessard, T. D. Terris, C. Dupuy, T. Baudin, Texture control of 316L parts by modulation of the melt pool morphology in selective laser melting, *Journal of Materials Processing Technology* 264 (2019) 21 – 31.

- [35] J.-Y. Kang, J. Yun, B. Kim, J. Choe, S. Yang, S.-J. Park, J.-H. Yu, Y.-J. Kim, Micro-texture analyses of a cold-work tool steel for additive manufacturing, *Materials* 13 (3) (2020) 788.
- [36] H. Kriaa, A. Guitton, N. Maloufi, Fundamental and experimental aspects of diffraction for characterizing dislocations by electron channeling contrast imaging in scanning electron microscope, *Scientific Reports* 7 (1) (2017) 1–8.
- [37] R. Miner, M. Castelli, Hardening mechanisms in a dynamic strain aging alloy, hastelloy x, during isothermal and thermomechanical cyclic deformation, *Material Transactions A* 23 (1992) 551–561.
- [38] W. Abuzaid, A. Oral, H. Sehitoglu, J. Lambros, H. J. Maier, Fatigue crack initiation in hastelloy x the role of boundaries, *Fatigue & Fracture of Engineering Materials & Structures* 36 (8) (2013) 809–826.
- [39] S. Pourbabak, M. L. Montero-Sistiaga, D. Schryvers, J. V. Humbeeck, K. Vanmeensel, Microscopic investigation of as built and hot isostatic pressed hastelloy x processed by selective laser melting, *Materials Characterization* 153 (2019) 366 – 371.
- [40] M. L. Montero-Sistiaga, S. Pourbabak, J. V. Humbeeck, D. Schryvers, K. Vanmeensel, Microstructure and mechanical properties of hastelloy x produced by hp-slm (high power selective laser melting), *Materials Design* 165 (2019) 107598.
- [41] D. N. Lee, K.-h. Kim, Y.-g. Lee, C.-H. Choi, Factors determining crystal orientation of dendritic growth during solidification, *Materials chemistry and physics* 47 (2-3) (1997) 154–158.
- [42] T. Ishimoto, K. Hagihara, K. Hisamoto, S.-H. Sun, T. Nakano, Crystallographic texture control of beta-type ti15mo5zr3al alloy by selective laser melting for the development of novel implants with a biocompatible low young’s modulus, *Scripta Materialia* 132 (2017) 34 – 38.
- [43] S. Bahl, S. Mishra, K. Yazar, I. R. Kola, K. Chatterjee, S. Suwas, Non-equilibrium microstructure, crystallographic texture and morphological texture synergistically result in unusual mechanical properties of 3d printed 316l stainless steel, *Additive Manufacturing* 28 (2019) 65 – 77.

- [44] R. R. Dehoff, M. M. Kirka, F. List, K. A. Unocic, W. J. Sames, Crystallographic texture engineering through novel melt strategies via electron beam melting: Inconel 718, *Materials Science and Technology* 31 (8) (2015) 939–944.
- [45] E. Hall, The deformation and ageing of mild steel: III discussion of results, *Physical Society of London* 64 (1951) 747 – 753.
- [46] N. Petch, The cleavage strength of polycrystals, *Journal of the Iron Steel Institute* 174 (1953) 25 – 28.
- [47] A. Thompson, Polycrystal hardening, in: *Work Hardening in Tension, Fatigue*, American Institute of Mining, Metallurgical, Petroleum Engineers, 1977, pp. 89 – 126.
- [48] J. DelValle, A. Picasso, R. Romero, Work-hardening in inconel X-750: study of stage II, *Acta Materialia* 46 (1998) 1981 – 1988.
- [49] C. Keller, E. Hug, D. Chateigner, On the origin of the stress decrease for nickel polycrystals with few grains across the thickness, *Materials Science and Engineering: A* 500 (1-2) (2009) 207 – 215.
- [50] E. Ma, Instabilities and ductility of nanocrystalline and ultrafine-grained metals, *Scripta Mater.* 49 (7) (2003) 663–668.
- [51] E. Ma, Eight routes to improve the tensile ductility of bulk nanostructured metals and alloys, *JOM* 58 (4) (2006) 49–53.